Northumbria Research Link

Northumbria University
NEWCASTLE

UniversityLibrary

Single Molecular Precursor Solution for CuIn(S,Se)₂ Thin Films Photovoltaic Cells: Structure and Device Characteristics

Devendra Tiwari,[†] Tristan Koehler,[§] Xianzhong Lin,[§] Andrei Sarua,[‡] Robert Harniman,[†] Lan Wang,[§] Reiner Klenk,[§] and David J Fermin*,[†]

[†]School of Chemistry, University of Bristol, Cantock's Close, Bristol BS8 1TS, United Kingdom

[‡]H.H. Wills Physics Laboratory, University of Bristol, Tyndall Avenue, Bristol BS8 1TL. United Kingdom

[§]Helmholtz-Zentrum Berlin für Materialien und Energie, Hahn-Meitner-Platz 1, D-14109 Berlin, Germany

S *Supporting Information*
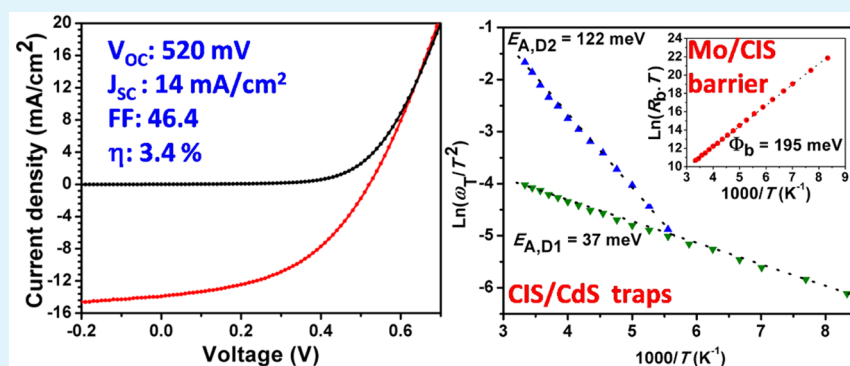
ABSTRACT: A single molecular precursor solution is described for the deposition of CuIn(S,Se)₂ (CIS) film onto Mo-coated glass substrates by spin coating, followed by annealing in Se atmosphere. Characterization of the films by X-ray diffraction, Raman spectroscopy and scanning electron microscopy demonstrates the formation of a highly homogeneous and compact 1.1 μm thick CIS layer, with a MoSe₂ under-layer. Atomic force microscopy reveals the presence of spherical grains between 400 and 450 nm, featuring surface corrugation in the range of 30 nm. Film composition is found to be in close agreement with that of the precursor solution. Diffuse reflectance spectroscopy shows a direct band gap (E_g) of 1.36 eV. Intensity and temperature dependence photoluminescence spectra show characteristic features associated with a donor−acceptor pair recombination mechanism, featuring activation energy of 34 meV. Over 85 solar cell devices with the configuration Mo/CIS/CdS/i-ZnO/Al:ZnO/Ni−Al and an total area of 0.5 cm² were fabricated and tested. The champion cell shows a power efficiency of 3.4% with an open circuit voltage of 521 mV and short circuit current of 14 mA/cm² under AM 1.5 illumination and an external quantum efficiency above 60%. Overall variation in each of solar cell parameters remains below 10% of the average value, demonstrating the remarkable homogeneity of this solution processing method. To understand the limitation of devices, the dependence of the open-circuit voltage and impedance spectra upon temperature were analyzed. The data reveal that the CuIn(S,Se)₂/CdS interface is the main recombination pathway with an activation energy of 0.79 eV as well as the presence of two "bulk" defect states with activation energies of 37 and 122 meV. We also estimated that the MoSe₂ under-layer generates back contact barrier of 195 meV.

KEYWORDS: *solar cells, CuIn(S,Se)₂, thin films, solution processing, recombination losses, impedance spectroscopy*

1. INTRODUCTION

Thin film technology is one of key contributor to global PV, occupying approximately 10% of the installed capacity. In addition to their suitability for flexible and building integrated PV, thin-film devices are characterized by a short energy payback time due to lower material purity and amounts required for efficient light harvesting.[1] Both Cu(In,Ga)(S,Se)₂- and CdTe-based technologies continue to show rise in their global module production. ZSW has recently reported 22.6% efficient CIGS solar cell, just surpassing the record efficiency for multicrystalline Si solar cells.[2] Historically, CIGS evolved out of CuInSe₂, where Ga is incorporated to broaden the composi-

tional range of PV active phase and improve device performance.[3−5] The initial success with CuInSe₂ and Cu(In,Ga)Se₂, led to evolution of their sulpho-selenides and sulfides, that is, CuIn(S,Se)₂, CuInS₂, and Cu(In,Ga)S₂.[6] Thus, CuIn(S_xSe$_{1−x}$)₂, CIS, and Cu(In,Ga)(S_xSe$_{1−x}$)₂, CIGS (commonly referred to as chalcopyrites), share similar material properties and processing.[6]

Conventionally, module production employs vacuum-based techniques, such as thermal evaporation or sputtering of metals, followed by reactive annealing under chalcogen atmosphere. While vacuum-based thin film deposition routes continue to be the benchmark and present choice for manufacturing, there has been a recent thrust in evolving toward nonvacuum deposition routes for multicomponent materials for solar cells.[7−10] The latter offers advantages of roll-to-roll processing and large area composition control with significantly lower capital investment. In general, three different strategies have been adopted for solution based growth of absorber layers: (i) electrodeposition/ electroplating and chemical bath deposition,[7,8,11] (ii) deposition from a slurry or suspension of nano/particulate precursors,[8,12−14] and (iii) deposition of molecular precursors.[8,15−20] Electrodeposition is a well-established route for high quality chalcopyrite solar cells; however, this method usually requires multiple deposition steps to control the composition of metals with vastly different reduction potentials. Nanoparticle precursor ink precursor has also led to efficient cells, although arduous and low-throughput synthesis and purification of nanoparticles call into question the scalability of this approach. Deposition of molecular precursors offers a simple approach with ease of tuning the composition and incorporation of dopant or surfactants in a single precursor solution.[10] With the appropriate rheology, solution precursors can be made suitable for a variety of low-cost and large scale coating methods, such as spray, inkjet, and slot-dyeing. For chalcopyrites, three different types of molecular precursors have been reported: (i) binary sulfides with excess chalcogen in hydrazine or thiol-amine solvent mixtures demonstrating efficiencies of 15.2% and 8.0% for CIGS and CIS, respectively,[15,16] (ii) metal precursors followed by annealing under chalcogen atmosphere, where a maximum efficiency of 11.3% for CIGS is achieved,[17−19] and (iii) single solution containing all metal precursors and thiourea as sulfur source.[20] The latter method is very appealing from the processing point of view and has shown remarkable efficiencies of 13.0% and 14.7% for CIS and CIGS respectively, with dimethyl sulfoxide (DMSO) used as solvent.[20]

In this contribution, we assess a new single molecular precursor based route employing dimethylformamide-isopropanol mixture (DMF-IPA) for the deposition of high quality $CuIn(S,Se)_2$ films. In comparison to DMSO, DMF is a highly versatile solvent enabling a 3-fold increase in the concentration of acidic inorganic precursors such as $InCl_3$ in comparison to DMSO (1.6 M in DMF in comparison to 0.45 M in DMSO). IPA reduces the surface tension of the precursor solution allowing an efficient spreading over areas as large as 5 × 5 cm² with only 0.1 mL. This property enables the formation of ∼1 μm CIS films with just 4 spin-coat steps. The films are characterized by grains in the micron-size range, with nanometer scale surface features. Under the specific processing conditions examined in this work, a band gap of 1.36 eV was obtained from diffuse reflectance measurements, which is consistent with 40% Se content. X-ray diffraction and Raman studies demonstrated highly crystalline materials, while the intensity and temperature dependence of the photoluminescence spectrum show the characteristic features of donor−acceptor recombination mechanism with activation energy of 34 meV. Devices with architecture SLG/Mo/CIS/CdS/i-ZnO/ Al:ZnO/Ni−Al were investigated, displaying power conversion efficiencies of up to 3.4% under AM1.5 illumination at room temperature. Impedance spectroscopy recorded as a function temperature demonstrated that key limiting factors in cell performance are the presence of defect states at the CIS/CdS interface and the formation of a $Mo(S,Se)_2$ layer during the thermal treatment.

2. RESULTS AND DISCUSSION

2.1. Structural and Optical Properties of CuIn(S,Se)₂ Film. Characteristic X-ray diffraction pattern of $CuIn(S,Se)_2$ films on Mo coated glass substrate, along with quantitative structure Rietveld refinement[21] is shown in Figure 1. As
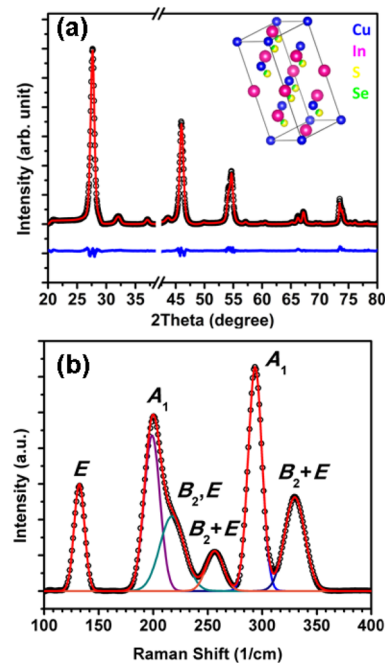

Figure 1. X-ray diffractogram and quantitative structure Rietveld refinement of $CuIn(S,Se)_2$ film obtained by a single molecular precursor solution (a). The inset shows a unit cell used for the structure refinement. The region between 37.5° and 40° were excluded from the figure due to the strong signal arising from the Mo substrate. Raman spectrum with different vibrational modes fitted with Voigt functions (b).

described in the Experimental Section, films are obtained by spin-coating a solution of chloride salts of Cu and In (1:1) ratio in DMF-IPA in the presence of thiourea, followed by annealing at 500 °C in the presence of Se powder. This procedure was inspired on our recent work on Cu_2ZnSnS_4 thin films.[22] The refinement statistical correlation factors R_p and R_{wp} converge to values of 8.28 and 10.02, respectively, indicating an excellent fit to the model structure. The material is found to crystallize in tetragonal chalcopyrite structure with lattice parameters $a = 5.6062(2)$ and $c = 11.3157(2)$ Å, corresponding to a tetragonal distortion factor $(c/2a)$ of 1.009. Crystal parameters are in good agreement with that of polycrystalline $CuIn(S,Se)_2$ samples synthesized by high temperature solid state synthesis.[23] No additional peaks corresponding to crystallographic phases other than chalcopyrite are identified. The Cu-chalcogen and In-chalcogen site interatomic distances have been estimated to be 2.383 and 2.490 Å, respectively, while the Cu−S−In bond angles around S centered tetrahedron varies between 108.98 and 109.62−113.38°. The occupancies of Cu site is 0.8824(5), and Se on chalcogen site 0.3773(4), suggest a Cu-poor and S rich composition. Energy dispersive analysis of X-rays (EDAX) performed over 45 different points across the 5 × 5 cm²

substrate showed average atomic ratios of Cu/In = 0.91 and Se/(S + Se) = 0.36, with a standard deviation of less than 1.6%. These compositions are consistent with the Rietveld analysis, demonstrating the highly homogeneous elemental composition achieved by this method. The broadening of diffraction peak indicates nanocrystalline nature of films, with an average crystallite size in the range of 30 nm as estimated from Debye−Scherrer relation.

The Raman spectrum of the $CuIn(S,Se)_2$ is shown in Figure 1b, in which the various vibrational modes were fitted to Voigt functions. The chalcopyrite structure belongs to D_{2d} point group with Raman active normal modes given by

$$\Gamma_{optical} = A_1 + 3B_1 + 3B_2 + 6E \qquad (1)$$

and

$$\Gamma_{acoustic} = B_2 + E \qquad (2)$$

On the basis of the Keating model, the peaks at 329 and 256 cm^{-1} are assigned to $B2$ symmetry, while peaks at 293, 217, 198, and 132 are assigned to A_1, E, A_1, and E symmetry, respectively.[24−26] No other peaks associated with secondary phases were identified. Consequently, XRD and Raman spectra consistently show the formation of phase pure chalcopyrite with slightly Cu deficient and sulfur rich composition.

The film morphology as probed by SEM and AFM is shown in Figure 2. The top-view SEM image (Figure 2a) shows a distribution of grain size ranging from 200 to 1000 nm. The SEM and the AFM images (Figure 2b) show that the surface of the grains is corrugated, with features in the range of 30 nm. A root-mean-square roughness of 60 nm can be estimated over an area of 10×10 μm^2. The length scale of the smallest features correlates with the mean crystallite size estimated by XRD. The cross-sectional SEM image in Figure 2c depicts uniform and adherent growth of CIS film across the substrate with a thickness of 1.1 μm over a 500 nm thick layer of Mo. Figure 2d shows an EDAX line scan measured across the red-line highlighted in cross-sectional view. Substantial concentrations of S and Se are seen within the top ∼250 nm of the Mo layer suggesting the formation of a $Mo(S,Se)_2$ film during the annealing step. This layer has strong implications on device functionality which will be discussed in later sections.

Figure 3a shows the diffuse reflectance spectrum of the CIS films between 800 and 1200 nm, featuring a sharp transition in reflectance with an onset at 850 nm. This sharp change in reflectance corresponds to band-to-band transition of the $CuIn(S,Se)_2$ film. Tauc plot obtained employing the Kubelka−Munk function (Figure S1) allowed estimating a $E_g = 1.36$ eV. The dependence of E_g on x in $CuIn(S_{1-x}Se_x)_2$ is determined by,

$$E_g = E_g(Se) + [E_g(S) - E_g(Se) - 1.25(1 - x)\Delta\chi]x \qquad (3)$$

where $\Delta\chi$ is the difference in Phillips electronegativity for Se (1.79) and S (1.89).[27] According to eq 3, a $E_g = 1.36$ eV corresponds to a 40% Se composition which is in excellent agreement with values obtained from EDAX and XRD.

Figure 3b displays the power dependent photoluminescence of the $CuIn(S,Se)_2$ film. The spectra show a broad peak centered at 1.27 eV. The photoluminescence intensity (I_{PL}) increases with the excitation power with a power law as indicated in Figure 3b. An exponent below unity along with the blue shift of the peak center with increasing pump power is manifestation of donor−acceptor pair (DAP) radiative recombination.[28,29] DAP transition energy is smaller than E_g
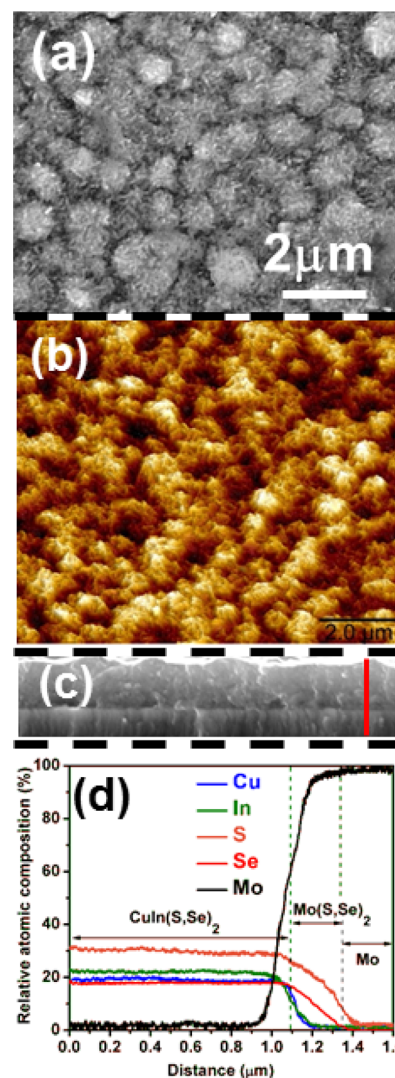

Figure 2. Surface topography of the $CuIn(S,Se)_2$ films obtained by SEM (a) and AFM (b). The scale range in (b) is 10 μm × 10 μm × 196 nm. Cross-sectional SEM image depicting a 1.1 μm $CuIn(S,Se)_2$ film on top of a 500 nm $Mo(S,Se)_2$ layer and Mo layer (c) and EDAX line scan depicting the relative atomic composition across the red-line in cross-sectional view (d).

by an energy factor associated with binding energy and Coulombic interaction of DA centers as described by eq 4

$$h\upsilon = E_g - E_A - E_D + \frac{e^2}{4\varepsilon\varepsilon_o R^2} \qquad (4)$$

where $h\upsilon$ is the emitted energy, E_A is the binding energy for acceptor, E_D is binding energy for donor, R is the distance between the donors and acceptors, and ε is the relative permittivity. Increasing the incident power generates extra carriers, reducing the distance and Columbic interaction between the DA centers. In addition, the slightly asymmetrical peak shape and considerable blue shift (6 meV/decade) upon increasing the incident power suggest the presence of electrostatic potential fluctuations. These fluctuations arise from local compositional inhomogeneity in the material and they are responsible for broadening of localized band gap states and band tailing.[29,30]
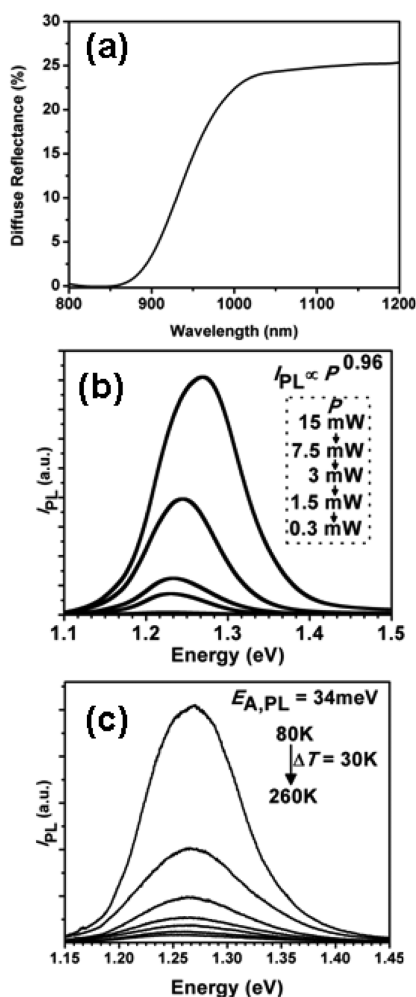
Figure 3. Room-temperature diffuse reflectance spectrum (a), power dependence of photoluminescence at room temperature (b) and temperature dependent photoluminescence (c) of the $CuIn(S,Se)_2$ film.
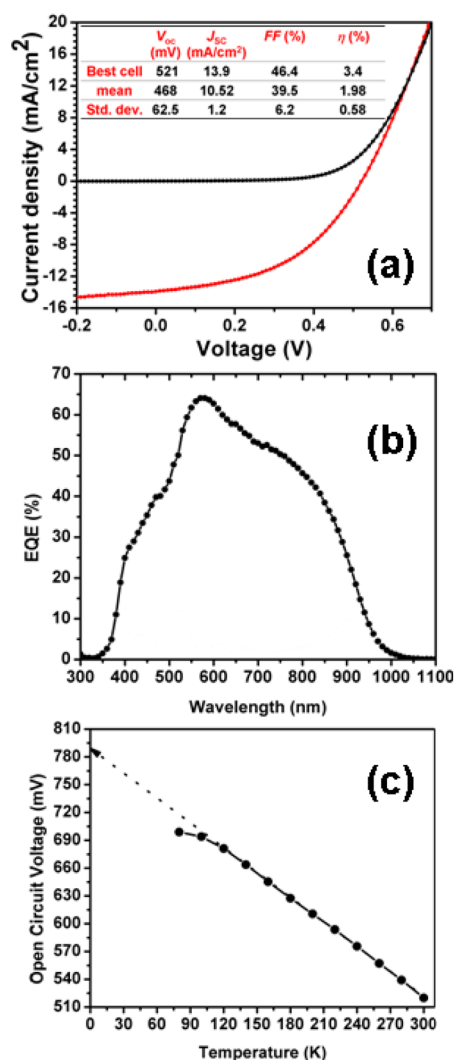

Figure 4. $J-V$ characteristics for best CIS device in the dark and under AM 1.5G illumination, inset showing variation in cell parameters: open-circuit voltage (V_{OC}), short-circuit current density (J_{SC}), fill factor (FF), and efficiency (η) for 82 devices (a), EQE spectrum (b), and temperature dependence of open-circuit voltage (V_{OC}) (c). Measurements are performed under front illumination at 23 °C on devices with structure: glass/Mo/CIS/CdS/i-ZnO/ZnO:Al/Ni−Al, with total area of 0.5 cm^2.

The PL maximum shifts to lower energies upon decreasing temperature by a factor of +0.95 meV/K as shown in Figure 3c. While DAP emission typically undergoes a blue shift with decreasing temperature, the red shift observed in these films is a result of the decrease in the ionization energy of deeper DA states due to the thermal ionization of shallower one. This behavior has been reported in the case of Cu-poor $CuIn(S,Se)_2$ films.[31] The activation energy ($E_{A,PL}$) of the DAP emission is obtained by fitting the integrated intensities of peaks versus temperature to a single exponential Arrhenius decay, yielding a value of 34 meV. Again, this value is consistent with previous studies on Cu-poor $CuIn(S,Se)_2$ ($S = 0.7$) and $CuInSe_2$.[23,31] These observations have been linked to DAP structures involving In_{Cu} donor states to V_{Cu} acceptor states, which is quite likely in present Cu-poor CIS films.[23,31,32]

2.2. Cell Performance.

The performance of devices featuring a substrate architecture, that is, glass/Mo/CIS/CdS/i-ZnO/Al:ZnO/Ni−Al architecture with a total area of 0.5 cm^2 is presented in Figure 4. $J-V$ characteristics of the best device in dark and under simulated AM 1.5G illumination, are shown in Figure 4a. The best cell displays a power conversion efficiency (η) of 3.4% with an open-circuit voltage (V_{OC}), short-circuit current (J_{SC}), and fill factor (FF) of 521 mV, 13.9 mA/cm^2, and 46.3%, respectively.

Variations in key device parameters, V_{OC}, J_{SC}, FF, and η, for 82 devices are included in the table inserted in Figure 4a. The data is characterized by a narrow distribution of cell parameters, in particular V_{OC} demonstrating excellent film homogeneity across the whole substrate area (5 × 5 cm^2). It is noticed that the light $J-V$ characteristics fails to comply with the shifting approximation and undergo a crossover under forward bias. Ideality factor (n) ≈ 2 under dark, suggest thermally activated recombination mechanism.[6,33] The device exhibits a moderate series resistance value which could be linked to the nanoscale corrugation of the film and the presence of a back contact barrier due to formation of $Mo(S,Se)_2$. The latter could also be responsible for a lower FF.

EQE spectrum of the best device is shown in Figure 4b, featuring a maximum value of 65% at 570 nm. The spectrum shows a steep increase in EQE up to ∼50% at the CIS absorption edge, followed by further rise to 65% between 850 to 650 nm and a sharp fall at the CdS absorption edge at 520

nm. A band gap of 1.35 eV is estimated from the first derivative near the CIS absorption edge, which matches well with values estimated from diffuse reflectance. The EQE also exhibits a weak red response in wavelengths between 850 and 650 nm, which is a well-established behavior arising from a limited diffusion length of carriers and high doping density in the absorber layer. As the wavelength is shifted to shorter values, light penetration depth decreases and carriers are generated closer to the CIS/CdS junction. For a finite carrier diffusion length, the probability of minority carrier reaching the CdS boundary increases, leading to an increase of the EQE value.[6]

Figure 4c shows the temperature dependence of V_{OC}, which can be described in terms of

$$eV_{OC} = E_{A,V_{oc}} - nk_B T \cdot \ln\left(\frac{J_{00}}{J_{SC}}\right) \tag{5}$$

where $E_{A,V_{oc}}$ is activation energy for the recombination, n is the ideality factor, and J_{00} is the temperature dependent prefactor of reverse saturation current.[33,34] Neglecting the temperature dependence of J_{00}, the plot in Figure 4c enables to estimate $E_{act,V_{oc}} = 0.79$ eV. The fact that $E_{act,V_{oc}}$ is significantly lower than E_g and $n \approx 2$ suggest surface recombination is the dominant path for carrier losses.[33,34] The temperature dependence of V_{OC} allows establishing the type of recombination present in the device. Given that $E_{A,V_{oc}} < E_g$ and $n > 2$ suggest that surface recombination is the dominant path for carrier losses.[33,34] The onset of V_{OC} saturation at temperatures below 100 K indicates freezing out of the dominant recombination pathway.

Further aspects linking device performance and material properties can be analyzed from the temperature dependence of the impedance spectra as illustrated in Figure 5. The data presented in Bode plots show a decrease in the low frequency impedance amplitude in the range of 10−100 kΩ (Figure 5a), while the frequency dependence of the phase (Figure 5b) indicated the presence of several time constants between 1 MHz and 20 Hz. The spectrum across the whole frequency range could be fitted satisfactorily by adopting the equivalent circuit shown in Figure 5c, featuring a series combination of a $R_b C_b$ associated with the back CIS/Mo barrier layer and a more complex set of elements associated with the active CIS/CdS layer. On the basis of previous impedance studies on chalcopyrite and CdTe devices,[35−37] the second impedance component contains $R_j C_j$ time constant corresponding to the active CIS/CdS junction, as well as additional elements associated with defect sites connected in parallel. We shall demonstrate further below that R_1, R_2, C_1, and C_2 elements described the dynamic behavior of trap states consistent with other independent observations. The continuous line in the Bode plots (Figures 5a and 5b) demonstrate the excellent fits using the equivalent circuit in Figure 5c, with the error converging below 5% across the whole frequency range.

Key parameters associated with the back contact and defect sites extracted from the impedance analysis as a function of temperature are shown in Figure 6. The series resistance R_s did not show any discernible temperature dependence and remains around 2.3 Ω cm². The temperature dependence of R_j and C_j are displayed in the Figure S2, with the latter being consistent with a doping density of the order of 10^{15} cm^{-3}. R_b, R_1, and R_2 show substantial increase with decreasing temperatures (Figure 6a), which can be rationalized in terms of tunneling assisted transport, characteristic of low mobility semiconductors. Figure
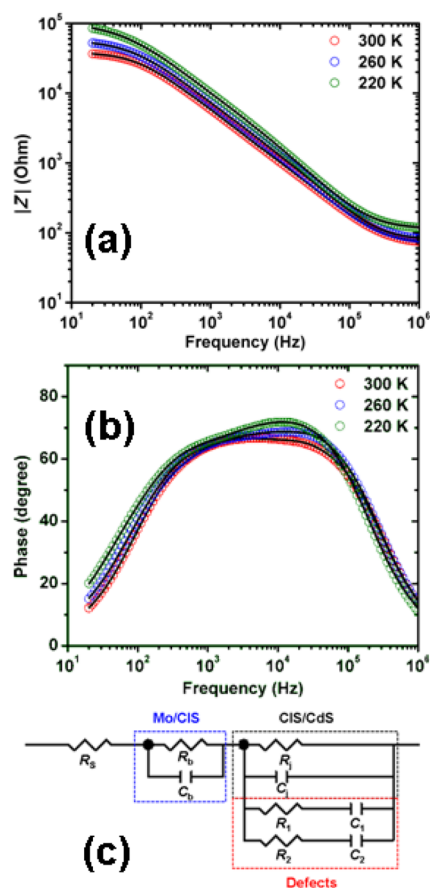

Figure 5. Impedance spectra of a CIS device ($\eta = 3\%$) showing the amplitude (a) and phase (b) as a function of temperature. The equivalent circuit used to analyze the spectra is shown in (c). Impedance spectra of the devices were recorded in the dark and at 0 V bias within a frequency range of 20 Hz to 1 MHz.

6b shows that capacitance associated with defect sites decreases with decreasing temperature. On the basis of these trends, a characteristic frequency associated with the trap state kinetics (estimated as $\omega_T = 1/RC$) can be examined as a function of temperature as shown in Figure 6c. The temperature dependence of ω_T can be expressed in terms of[35]

$$\omega_T = \xi_o T^2 \cdot \exp\left(\frac{E_{A,D}}{k_B T}\right) \tag{6}$$

where ξ_0 is the thermal emission factor and $E_{A,D}$ is the activation energy of the defect. From the slopes in Figure 6c, it can be estimated activation energies for the defect levels as $E_{A,D1} = 37.5$ meV and $E_{A,D2} = 122$ meV. The value of $E_{A,D1}$ is remarkably close to the activation energy donor−acceptor state obtained from the temperature-dependent PL (see Figure 3). This defect level, commonly denoted as α in the chalcopyrite literature, is generally assigned to acceptors originating from V_{Cu} level.[15,38,39] On the other hand, $E_{A,D2}$ is similar to the value associated with N_1 states which have been attributed to interface states present at the CIS/CdS interface.[38,39] As the potential bias mostly develops at the CIS/CdS junction, the dynamic of electron population at trap states is rather sensitive to the ac potential perturbation.[40] It has also been shown that N_1 states are present even upon replacing CdS by InS$_x$, suggesting that the defect is associated with the CIS surface.[40] In our devices, the highly textured surface of CIS will promote a
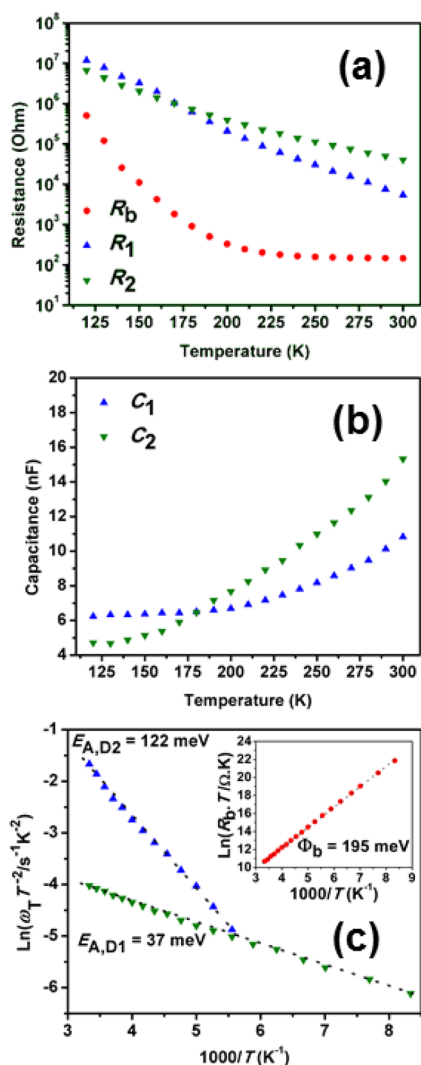
Figure 6. Temperature dependence of resistances (a) associated with the Mo/CIS junction (R_b) and defect states (R_1 and R_2), as well as the corresponding C_b, C_1, and C_2 capacitances values (b) extracted from impedance spectra of the devices in the dark. Arrhenius plot for determination of activation energies of defect states with inset showing the plot $\ln(R_b T)$ vs T for estimation of back contact barrier height (c).

large density of N_1 states, increasing carrier shunting paths (moderate shunt resistance) and low $E_{A,V_{oc}}$ values with respect to E_g. We could exclude secondary phases and pin-holes as a major contributor to the shunting paths in view of the highly compact and phase pure nature of the films as revealed by SEM, XRD EDAX, and Raman spectroscopy.

The temperature dependence of the back contact resistance at the Mo/CIS junction can be described in terms of[15,36]

$$R_b = \frac{k_B}{eA^*T} \cdot \exp\left(\frac{\Phi_b}{k_B T}\right) \qquad (7)$$

where A^* is the effective Richardson's constant and ϕ_b is the back contact barrier height. Plotting $\ln(R_b T)$ versus T (inset in Figure 6c) allows estimating ϕ_b = 195 meV.

In summary, the device J–V curves, EQE, and temperature-dependent impedance spectra strongly suggest that defect states present at grain boundaries at the CIS/CdS junction are the key limiting factor in the efficiency of the device, along with the

electronic barrier at the Mo/CIS junction. These factors predominantly affect the J_{SC} and FF values. Consequently, it is crucial to design barrier layers that avoid selenization of the Mo substrate during the annealing step. This would enable to tune the annealing conditions in order to decrease grain boundaries at CIS/CdS junction, minimizing surface recombination losses.

3. CONCLUSIONS

We describe a new methodology for processing high quality $CuIn(S,Se)_2$ by spin coating of a single molecular precursor solution based on DMF-IPA mixtures. Deposition and reactive thermal annealing in the presence of Se generate single phase CIS films featuring Cu-poor and S-rich compositions, with a E_g = 1.36 eV. Temperature-dependence PL measurements are characterized by a donor–acceptor recombination mechanism with activation energy of 34 meV. Thin film devices with total areas of 0.5 cm^2 exhibited efficiencies up to 3.4%. Statistical analysis of the various cell parameters shows a small variation across the whole substrate area (5 × 5 cm^2). Temperature dependence impedance spectroscopy in the dark showed characteristic dynamic responses associated with two defect states as well as the interfacial layer generated by selenization of the Mo surface. One of the states exhibited identical activation energy to the radiative recombination dominating the PL response. The activation energies of the defect levels (so-called α and N_1 states) are similar to those reported in high quality CIS devices exhibiting efficiencies above 15%.[15] Consequently, the key limiting factor in our devices is not the nature but potentially the density of these defect states. Considering that some of these states have been linked to grain boundaries, it is crucial to improve the mean grain sizes obtained by our methodology. This involves not only optimization of the annealing step but also passivation of the Mo surface to limit the extent of substrate selenization.

4. EXPERIMENTAL SECTION

The $CuIn(S,Se)_2$ are deposited on to 5 × 5 cm^2 Mo-coated glass substrate (MSolv) using a approach similar to processing used for Cu_2ZnSnS_4 films and devices reported previously.[22] No blocking layer between Mo and glass is employed in order to minimize Na diffusion from substrates to absorber. CIS films are deposited by spin-coating a DMF-IPA (1:1) solution of Cu(II) and In(III) chloride (with an equimolar concentration of 1.6 M), as well as thiourea at 2000 rpm, followed by heating at 300 °C in air for 2 min. This step is repeated 4 times to achieve a final thickness slightly larger than 1 μm. The films are subsequently placed in a graphite box with 100 mg of selenium powder for annealing. Annealing is performed in a MTI-OTF1200X furnace with a ramping of 10 °C/s to 500 °C, dwelling at 500 °C for 30 min and cooling naturally, exhausting all the selenium. Prior to the buffer layer deposition, the as-annealed films are etched in a 10% KCN (aq.) solution. Immediately after annealing, the CdS layer is grown by chemical bath deposition employing CdSO$_4$, thiourea and ammonium hydroxide, at 70 °C. The devices are completed by RF-sputtering an i-ZnO (50 nm) and Al-doped ZnO window layer (350 nm), followed by evaporation of Ni/Al contact grid using a shadow mask. Total area of a cell is defined by mechanically scribing a 0.5 cm × 1.0 cm rectangular area from an array of 32 cells on 5 cm × 5 cm support. The shadowing generated by the top metallic contact is not considered in the measurements and no antireflection coating was used. J–V plots were measured in dark and under illumination with simulated AM 1.5 G spectrum (in-house class A solar simulator) and integrated power density of 100 mW/cm^2 at 23 °C. The solar simulator has a homogeneous and collimated illumination area of 17.5 cm × 17.5 cm and a temperature controlled area of 11.5 cm × 11.5 cm in the center. The measurements are performed by placing the sample in the center.

The illumination divergence over such small area of cell with an area of 0.5 cm^2 is considered to be negligible. A total of 125 points were measured by scanning the voltage from 0.75 to −0.5 V, with no evidence of hysteresis observed (as expected for this fully inorganic solid-state devices). The external quantum efficiency (EQE) was recorded employing halogen and Xe lamps with a Bentham TM 300 monochromator (Bentham instruments). ISE-Fraunhofer certified Si and Ge cells are used as the reference for both $J-V$ and EQE measurements. The mismatch factor between the tested and reference cell was found to be 0.9756. Low-temperature impedance measurements are carried out under dark using a Solatron Modulab impedance analyzer, interfaced with Linkam HFS 600PB4 cooling stage, in frequency range of 20 Hz to 1 MHz with no applied DC bias and AC stimulus of 25 mV.

■ ASSOCIATED CONTENT

Ⓢ Supporting Information

The Supporting Information is available free of charge on the ACS Publications website at DOI: 10.1021/acsami.6b12306.

> Film characterization details, modified Tauc plot from diffuse reflectance for estimating band gap, and temperature variation of CIS/CdS capacitance, C_j, and resistance, R_j (PDF)

■ AUTHOR INFORMATION

Corresponding Author

*E-mail: david.fermin@bristol.ac.uk.

ORCID Ⓘ

Andrei Sarua: 0000-0001-5617-4227

David J Fermin: 0000-0002-0376-5506

Notes

The authors declare no competing financial interest.

■ ACKNOWLEDGMENTS

■ REFERENCES

(1) Fraunhofer Institute for Solar Energy Systems, *Photovoltaics Report*; Freiburg, 6 June 2016.

(2) Jackson, P.; Wuerz, R.; Hariskos, D.; Lotter, E.; Witte, W.; Powalla, M. Effects of Heavy Alkali Elements in Cu(In,Ga)Se$_2$ Solar Cells with Efficiencies up to 22.6%. Phys. *Phys. Status Solidi RRL* **2016**, *10*, 583−586.

(3) Herberhotz, R.; Schock, H. W.; Rau, U.; Werner, J. H.; Haalboom, T.; Godecke, T.; Ernst, F.; Beilharz, C.; Benz, K. W.; Cahen, D. New Aspects of Phase Segregation and Junction Formation in CuInSe2. *Conf. Rec. Twenty Sixth IEEE Photovolt. Spec. Conf.* **1997**, 323−326.

(4) Jensen, C. L.; Tarrant, D. E.; Ermer, J. H.; Pollock, G. A. The Role of Gallium in CuInSe2 Solar Cells Fabricated by a Two-Stage Method. *Conf. Rec. Twenty Third IEEE Photovolt. Spec. Conf.* **1993**, 577−580.

(5) Stanbery, B. J. Copper Indium Selenides and Related Materials for Photovoltaic Devices. *Crit. Rev. Solid State Mater. Sci.* **2002**, *27*, 73−117.

(6) Scheer, R.; Schock, H. *Chalcogenide Photovoltaics*; Wiley-VCH: Weinheim, Germany, 2011.

(7) Romanyuk, Y. E.; Hagendorfer, H.; Stücheli, P.; Fuchs, P.; Uhl, A. R.; Sutter-Fella, C. M.; Werner, M.; Haass, S.; Stückelberger, J.; Broussillou, C.; Grand, P. P.; Bermudez, V.; Tiwari, A. N. All Solution-Processed Chalcogenide Solar Cells - From Single Functional Layers Towards a 13.8% Efficient CIGS Device. *Adv. Funct. Mater.* **2015**, *25*, 12−27.

(8) Azimi, H.; Hou, Y.; Brabec, C. J. Towards Low-Cost, Environmentally Friendly Printed Chalcopyrite and Kesterite Solar Cells. *Energy Environ. Sci.* **2014**, *7*, 1829−1849.

(9) Hibberd, C. J.; Chassaing, E.; Liu, W.; Mitzi, D. B.; Lincot, D.; Tiwari, A. N. Non-Vacuum Methods for Formation of Cu(In, Ga) (Se, S)2 Thin Film Photovoltaic Absorbers. *Prog. Photovoltaics* **2010**, *18*, 434−452.

(10) Todorov, T.; Mitzi, D. B. Direct Liquid Coating of Chalcopyrite Light-Absorbing Layers for Photovoltaic Devices. *Eur. J. Inorg. Chem.* **2010**, *2010*, 17−28.

(11) Bhattacharya, R. N.; Kim, Y.; Yoon, S.; Jeon, M. Electro-deposited CIS and CIGS-Based Solar Cells. *ECS Trans.* **2013**, *50*, 23−30.

(12) Norsworthy, G.; Leidholm, C. R.; Halani, A.; Kapur, V. K.; Roe, R.; Basol, B. M.; Matson, R. CIS Film Growth by Metallic Ink Coating and Selenization. *Sol. Energy Mater. Sol. Cells* **2000**, *60*, 127−134.

(13) Jeong, S.; Lee, B.-S.; Ahn, S.; Yoon, K.; Seo, Y.-H.; Choi, Y.; Ryu, B.-H. An 8.2% Efficient Solution-Processed CuInSe$_2$ Solar Cell Based on Multiphase CuInSe$_2$ Nanoparticles. *Energy Environ. Sci.* **2012**, *5*, 7539.

(14) Cho, A.; Ahn, S.; Yun, J. H.; Gwak, J.; Song, H.; Yoon, K. A Hybrid Ink of Binary Copper Sulfide Nanoparticles and Indium Precursor Solution for a Dense CuInSe$_2$ Absorber Thin Film and Its Photovoltaic Performance. *J. Mater. Chem.* **2012**, *22*, 17893.

(15) Todorov, T. K.; Gunawan, O.; Gokmen, T.; Mitzi, D. B. Solution-Processed Cu(In,Ga)(S,Se)$_2$ Absorber Yielding 15.2% Efficient Solar Cell. *Prog. Photovoltaics* **2013**, *21*, 82−87.

(16) Arnou, P.; van Hest, F. A. M.; Cooper, C.; Malkov, A. V.; Walls, J.; Bowers, J. Hydrazine-Free Solution Deposited CuIn(S,Se)$_2$ Solar Cells by Spray Deposition of Metal Chalcogenides. *ACS Appl. Mater. Interfaces* **2016**, *8*, 11893−11897.

(17) Lin, X.; Klenk, R.; Wang, L.; Koehler, T.; Albert, J.; Fiechter, S.; Ennaoui, A.; Lux-Steiner, M. 11.3% Efficient Cu(In,Ga)(S,Se)$_2$ Thin Film Solar Cells by Drop-on-Demand Inkjet Printing. *Energy Environ. Sci.* **2016**, *9*, 2037−2043.

(18) Kaelin, M.; Rudmann, D.; Kurdesau, F.; Zogg, H.; Meyer, T.; Tiwari, A. N. Low-Cost CIGS Solar Cells by Paste Coating and Selenization. *Thin Solid Films* **2005**, *480−481*, 486−490.

(19) Wang, G.; Wang, S.; Cui, Y.; Pan, D. A Novel and Versatile Strategy to Prepare Metal-Organic Molecular Precursor Solutions and Its Application in Cu(In,Ga)(S,Se)$_2$ Solar Cells. *Chem. Mater.* **2012**, *24*, 3993−3997.

(20) Uhl, A. R.; Katahara, J. K.; Hillhouse, H. W. Molecular-Ink Route to 13.0% Efficient Low-Bandgap CuIn(S,Se)$_2$ and 14.7% Efficient Cu(In,Ga)(S,Se)$_2$ solar Cells. *Energy Environ. Sci.* **2016**, *9*, 130−134.

(21) Rodriguez-Carvajal, J. FULLPROF: A Program for Rietveld Refinement and Pattern Matching Analysis. *Abstracts of the Satellite Meeting on Powder Diffraction of the XV Congress of the IUCr* **1990**, 127.

(22) Tiwari, D.; Koehler, T.; Lin, X.; Harniman, R.; Griffiths, I.; Wang, L.; Cherns, D.; Klenk, R.; Fermin, D. J. Cu$_2$ZnSnS$_4$ Thin-Films Generated from a Single Solution Based Precursor: The Effect of Na and Sb Doping. *Chem. Mater.* **2016**, *28*, 4991−4997.

(23) Zeaiter, K.; Llinares, Y.; Llinarès, C. Structural and Photo-luminescence Study of the Quaternary Alloys System CuIn(S$_x$Se$_{1-x}$)$_2$. *Sol. Energy Mater. Sol. Cells* **2000**, *61*, 313−329.

(24) Keating, P. N. Effect of Invariance Requirements on the Elastic Strain Energy of Crystals with Application to the Diamond Structure. *Phys. Rev.* **1966**, *145*, 637−645.

(25) Alvarez-Garcia, J.; Barcones, B.; Perez-Rodriguez, A.; Romano-Rodriguez, A.; Morante, J. R.; Janotti, A.; Wei, S. H.; Scheer, R. Vibrational and Crystalline Properties of Polymorphic $CuInC_2$ (C = Se,S) Chalcogenides. *Phys. Rev. B: Condens. Matter Mater. Phys.* **2005**, *71*, 054303.

(26) Bacewicz, R.; Gebicki, W.; Filipowicz, J. Raman Scattering in $CuInS_{2x}Se_{2(1-x)}$ Mixed Crystals. *J. Phys.: Condens. Matter* **1994**, *6*, L777−L780.

(27) Tinoco, T.; Quintero, M.; Rincón, R. Variation of the Energy Gap with Composition in $AIBIIIC_2VI$ Chalcopyrite-Structure Alloys. *Phys. Rev. B: Condens. Matter Mater. Phys.* **1991**, *44*, 1613−1615.

(28) Schmidt, T.; Lischka, K.; Zulehner, W. Excitation-Power Dependence of the near-Band-Edge Photoluminescence of Semiconductors. *Phys. Rev. B: Condens. Matter Mater. Phys.* **1992**, *45*, 8989−8994.

(29) Grossberg, M.; Krustok, J.; Timmo, K.; Altosaar, M. Radiative Recombination in $Cu_2ZnSnSe_4$ Monograins Studied by Photoluminescence Spectroscopy. *Thin Solid Films* **2009**, *517*, 2489−2492.

(30) Oueslati, S.; Brammertz, G.; Buffiere, M.; Koeble, C.; Oualid, T.; Meuris, M.; Poortmans, J. Photoluminescence Study and Observation of Unusual Optical Transitions in $Cu_2ZnSnSe_4$/CdS/ZnO Solar Cells. *Sol. Energy Mater. Sol. Cells* **2015**, *134*, 340−345.

(31) Zott, S.; Leo, K.; Ruckh, M.; Schock, H. W. Radiative Recombination in $CuInSe_2$ Thin Films. *J. Appl. Phys.* **1997**, *82*, 356−367.

(32) Wasim, S. M. Transport Properties of CuInSe2. *Sol. Cells* **1986**, *16*, 289−316.

(33) Kirchartz, T.; Rau, U.; Abou-Ras, D. *Advanced Characterization Techniques for Thin Film Solar Cells*; Wiley-VCH: Weinheim, Germany, 2011.

(34) Tiwari, D.; Fermin, D. J.; Chaudhuri, T. K.; Ray, A. Solution Processed Bismuth Ferrite Thin Films for All-Oxide Solar Photovoltaics. *J. Phys. Chem. C* **2015**, *119*, 5872−5877.

(35) Fernandes, P. A.; Sartori, A. F.; Salome, P. M. P.; Malaquias, J.; Da Cunha, A. F.; Graça, M. P. F.; Gonzalez, J. C. Admittance Spectroscopy of Cu_2ZnSnS_4 Based Thin Film Solar Cells. *Appl. Phys. Lett.* **2012**, *100*, 233504.

(36) Proskuryakov, Y. Y.; Durose, K.; Taele, B. M.; Oelting, S. Impedance Spectroscopy of Unetched CdTe/CdS Solar Cells-Equivalent Circuit Analysis. *J. Appl. Phys.* **2007**, *102*, 024504−1−11.

(37) Strifler, W. A.; Bates, C. W. Admittance Spectroscopy of $CuInSe_2$/CdS Solar Cells Prepared by Chemical Spray Pyrolysis. *J. Appl. Phys.* **1992**, *71*, 4358−4364.

(38) Krustok, J.; Danilson, M.; Jagomägi, A.; Grossberg, M.; Raudoja, J. Device Characteristics of $CuInSe_2$ Based Solar Cells. *Proc. SPIE* **2006**, *5946*, 236−242.

(39) Walter, T.; Herberholz, R.; Müller, C.; Schock, H. W. Determination of Defect Distributions from Admittance Measurements and Application to Cu(In,Ga)Se$_2$ Based Heterojunctions. *J. Appl. Phys.* **1996**, *80*, 4411−4420.

(40) Herberholz, R.; Igalson, M.; Schock, H. W. Distinction between Bulk and Interface States in $CuInSe_2$/CdS/ZnO by Space Charge Spectroscopy. *J. Appl. Phys.* **1998**, *83*, 318.